

Copper-Capped Carbon Nanocones on Silicon: Plasma-Enabled Growth Control

Shailesh Kumar,^{†,‡,⊥} Igor Levchenko,^{*,†,‡,⊥} David Farrant,[†] Michael Keidar,[§] Holger Kersten,^{||} and Kostya (Ken) Ostrikov^{†,‡}

[†]Plasma Nanoscience Centre Australia (PNCA), CSIRO Materials Science and Engineering, P.O. Box 218, Lindfield, NSW 2070, Australia

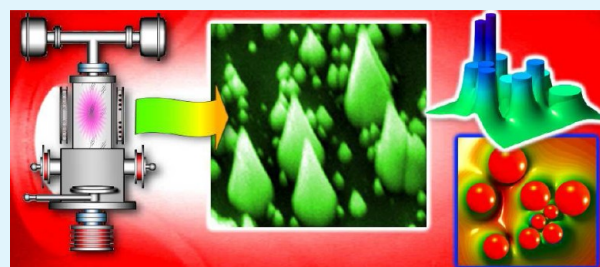
[‡]Plasma Nanoscience, School of Physics, The University of Sydney, Sydney, NSW 2006, Australia

[§]Department of Mechanical and Aerospace Engineering, The George Washington University, Washington, DC 20052, United States

^{||}Institute of Experimental and Applied Physics, University Kiel, D-24098 Kiel, Germany

ABSTRACT: Controlled self-organized growth of vertically aligned carbon nanocone arrays in a radio frequency inductively coupled plasma-based process is studied. The experiments have demonstrated that the gaps between the nanocones, density of the nanocone array, and the shape of the nanocones can be effectively controlled by the process parameters such as gas composition (hydrogen content) and electrical bias applied to the substrate. Optical measurements have demonstrated lower reflectance of the nanocone array as compared with a bare Si wafer, thus evidencing their potential for the use in optical devices. The nanocone formation mechanism is explained in terms of redistribution of surface and volumetric fluxes of plasma-generated species in a developing nanocone array and passivation of carbon in narrow gaps where the access of plasma ions is hindered. Extensive numerical simulations were used to support the proposed growth mechanism.

KEYWORDS: carbon nanocones, catalyst, plasma, self-organization, optical properties, sensing



1. INTRODUCTION

The vertically aligned self-assembled surface-grown nanostructures such as nanotubes, nanocones, nanorods, and others demonstrate many unique electrical, mechanical, magnetic, and other properties making them a very promising platform for various applications such as electron emission-based nanodevices, nanoelectronics, nanomechanical nanodevices, environment monitoring equipment, biosensors, scanning probe microscopes, etc.^{1–4} To stay up-to-date, these devices should demonstrate exceptional properties and thus, the fabrication process should be highly controllable to ensure formation of the nanostructures with the predictable crystalline structure, chemical composition, and geometrical shape.^{5–7} The nanofabrication process is very complicated, and thus, a deep understanding of the numerous physical effects and mechanisms involved in the growth is critical for the efficient implementation of the vertically aligned self-assembled nanostructures in modern nanodevices.^{8–10}

The existing technologies used to fabricate vertically aligned nanostructures can be split into the two main categories, namely, neutral-based and plasma-based processes. Chemical vapor deposition (CVD) is one of the most widely used production methods based on the neutral process environment for the production of vertically aligned carbon nanostructures. Nevertheless, CVD shows a significant lack of controllability in the shape and structure of the nanostructures assembled by the

CVD. In contrast, the processes based on low-temperature plasmas demonstrate relatively high controllability, due to the possibility to control the nanostructure growth by the process parameters such as the electron temperature, plasma density, and substrate bias.¹¹ Some applications, in particular those based on the use of a single, free-standing nanostructure (i.e., microscope probes or elements of the micro- and nanomechanical devices), pose additional requirements to the vertical nanostructures. Ideally, those nanostructures should be made of a highly conductive material and simultaneously, they should be capped with a highly conductive metal. Special requirements are also imposed on the shape, position, and area density of the nanostructures. Among others, carbon nanocones are the best candidates for such applications due to the high conductivity and thermal stability of sp² carbon. Nevertheless, they usually exhibit the base-growth mode, with the catalyst nanoparticles attached to the substrate surface and supplying building material to the growing nanostructures through carbon diffusion in metals with a very high carbon solubility, such as Ni, Co, etc.¹² Thus, in this case the metal cap is not formed on the nanostructure top. As a result, the top is rounded and what is more important, it cannot endure the high thermal and

Received: August 17, 2012

Accepted: October 12, 2012

Published: October 12, 2012

mechanical load. Besides, the formation of the free-standing nanostructures is also a problem for the base-growth mode. When the metal catalyst nanoparticles placed closely to each other on the surface, the growing nanostructures coalesce and produce large structures with irregular shape.

Recently, we have reported on the successful growth of long, vertically aligned, clearly separated carbon nanocones with copper caps on the tops.¹³ In this paper, we study the dependence of the nanocone array morphology on the process parameters, namely, gas composition (by changing nitrogen and hydrogen content), and ion energy which was varied by changing the surface bias. Besides, we demonstrate that the results of the spectral reflectance measurements imply possible applications of the nanocone arrays in optical devices. We have also developed a sophisticated model and conducted numerical simulations which support the proposed growth model.

This paper is organized as follows. The main experimental details of carbon nanocone fabrication and characterization are described in section 2. In section 3 we describe the obtained results, with special attention paid to the dependence of the nanocone array characteristics on the process parameters. The results of the optical measurements are also presented, which have demonstrated that the surface covered with the copper-capped carbon nanocones has lower reflectance in the visible light range. In section 4 we introduce the numerical model and the results of multiscale hybrid simulations of the development of nanocone arrays in the plasma and discuss the obtained results. A growth model was supported by the numerical calculations which confirmed the possibility of the separated growth of the closely located nanostructures in the low-temperature plasmas. The article concludes with a brief summary of the results obtained and the outlook for future research.

2. EXPERIMENTAL SECTION

The nanocones were grown in the low-temperature plasma produced by the radio frequency inductively coupled plasma (ICP) reactor, on the Si(100) surface. Scanning electron microscopy (SEM), transmission electron microscopy (TEM), energy-dispersive X-ray spectroscopy (EDS), and Raman characterization techniques were used to reveal the size, shape, chemical composition, internal structure, and properties of the carbon nanocones. The experiment was conducted in a hybrid ICP-magnetron system operating at 13.56 MHz radio frequency (rf). The plasma was generated in a quartz tube with a diameter of 10 cm and with the help of a helical water-cooled rf coil installed outside the tube. In addition to the ICP plasma source, two direct current (dc) magnetrons were installed oppositely in the stainless steel chamber, thus providing the deposition of metal films simultaneously with or prior to the ICP treatment. During the process, a negative dc bias of -50 to -100 V was supplied to the substrate holder. A gas system consisting of the gas bottles and automated mass flow controller system ensured the nitrogen and methane supply with an accuracy of 1%. Rotary and turbo-molecular vacuum pumps were able to sustain a base pressure of 0.01 Pa. Figure 1a shows a schematic of the experimental setup, and Figure 1b is the photograph of the dc magnetron discharge. Some more details of the setup and its characteristics can be found elsewhere.¹⁴

We used a three-stage fabrication process, which was conducted *in vacuo* in the above-described hybrid ICP-magnetron system. Because of the presence of dc magnetrons, it was possible to carry out the whole three-stage process in the same vacuum cycle. Thus, oxidation and contamination from the air was avoided. At the first stage of the process, we used a dc magnetron with a copper target to deposit a continuous thin copper film with the thickness of 8–10 nm on a Si(100) wafer. Immediately after that, without breaching vacuum in the treatment chamber, the copper film was processed for 5 min in the

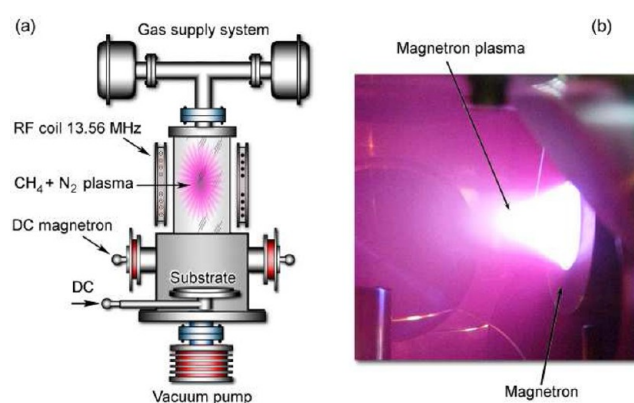


Figure 1. Scheme of the hybrid ICP-magnetron setup comprising the gas supply system, two dc magnetrons and ICP plasma source (a) and photo of the magnetron discharge (b) used for the meal catalyst application to the silicon substrate.

ICP plasma ignited in pure nitrogen. During this treatment, the rf power level was set to 500 W, nitrogen pressure was 4.0 Pa, and the substrate was negatively biased with -25 V dc. Under the bombardment of ions extracted from the plasma, the copper film was fragmented into an array of copper nanoparticles with a mean size of 20–50 nm. Next, the nanocone synthesis was started for 15 min by supplying the gas mixture ($\text{CH}_4 + \text{N}_2$, with the CH_4/N_2 ratio of 1:1) and igniting the ICP plasma at 15 Pa of the chamber pressure and 800 W of the rf input power (reference experiment). During the nanocone synthesis, the substrate was biased with -50 V voltage. No external substrate heating was used, and the surface temperature was maintained at about 500 °C in the N_2 plasma and about 600 °C in the $\text{CH}_4 + \text{N}_2$ plasma. No nanostructures were found after the additional experiment conducted in a $\text{CH}_4 + \text{N}_2$ gas mixture at the same pressure and surface temperatures, thus confirming that the plasma environment was essential for this low-temperature nanofabrication process. Indeed, typical temperatures required for the plasma-free furnace synthesis of carbon nanostructures reach 1000 °C.^{15,16}

To further investigate the effect of the process parameters on the structure and morphology of the carbon nanostructures, we have performed similar experiments using a modified environment (hydrogen-contained $\text{CH}_4/\text{H}_2/\text{N}_2$ gas mixtures with the ratios 50/30/20, 50/10/40, and 40/0/60 were used) and two additional, 0 and -100 V dc biases. More experiment details can be found in our previous publications.^{13,17}

3. RESULTS AND DISCUSSION

3.1. Structure and Characterization of Nanocone Arrays. At the first stage of the process, magnetron sputtering was used to form a continuous and homogeneous copper layer with the thickness of several (up to 10 nm) was formed on the silicon substrate, as confirmed by the profilometer measurements and SEM examination. At the second stage, ICP plasma treatment in the nitrogen environment for 5 min resulted in the fragmentation of the continuous copper film and finally in the formation of the self-organized irregular array of copper nanoparticles with a mean size of 50 nm due to the surface heating and surface diffusion-driven processes. At the third stage, the carbon nanocones were formed. Detailed SEM and TEM characterization of the typical copper-capped carbon nanocones synthesized in the reference experiment ($\text{CH}_4 + \text{N}_2$ ratio 1:1, ICP plasma at 15 Pa and 800 W) are shown in Figure 2. Low- and medium-magnification SEM images (a, b) show the groups of the nanocones and isolated nanostructures on the substrate surface, covered with small “second generation”

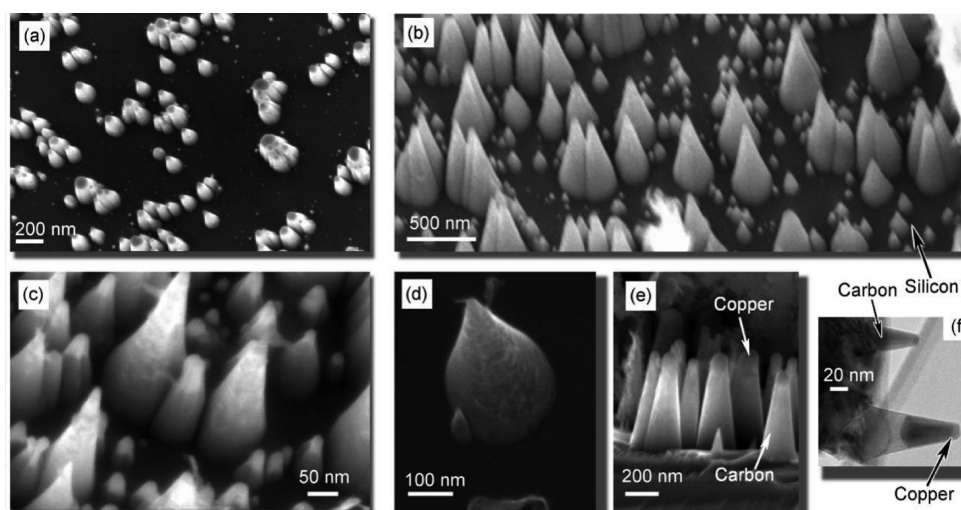


Figure 2. SEM and TEM images of the typical copper-capped carbon nanocones grown on a silicon wafer. The low-magnification SEM image (a) shows the groups of the nanocones, alongside with the isolated nanostructures. The medium-magnification image (b) shows that the substrate surface between the grown nanocones is covered with small “second-generation” structures. High-magnification images show the narrow gaps formed by the closely grown nanocones (c) and the near-perfect conical shape of the single nanocone (d). The side-view SEM image (e) shows the shape of the copper caps on the nanocones. The TEM image (f) confirms the structure (carbon base and copper cap) of the typical nanocone found on the substrate.

structures between the larger nanocones. The nanocones have a height of up to 500 nm and a base diameter of about 150 nm.

High-magnification image of the array (part c) shows that the close-located nanocones did not merge but form narrow gaps between them. The near-perfect conical shape of a single nanocone is seen in Figure 2d. The nanocone is topped with a massive, round-shaped copper cap with the top radius of approximately 10 nm and the length reaching 100 nm (side-view SEM image illustrating the shape of the cap is shown in Figure 2e). The TEM image (part f) confirms the structure (carbon base and copper cap) of a typical nanocone.

To check the chemical composition of the copper-capped nanocones, we have taken EDS spectra from the nanocone base and nanocone top (Figure 3). With the EDS spot pointed to the nanocone base, the EDS spectrum showed the presence of carbon and silicon (a signal originating from the substrate material, Figure 3a,b). With the EDS spot pointed to the nanocone cap, a strong copper signal was obtained thus

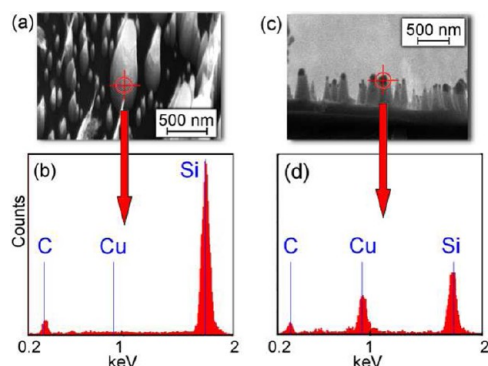


Figure 3. Side view of the nanocones and the corresponding EDS spectra. With the EDS spot on the nanocone base (a), the EDS spectrum shows the presence of carbon and silicon (substrate material) (b). With the EDS spot on the nanocone cap (c), the presence of copper is evidenced.

evidencing the presence of copper at the nanocone top (Figure 3c,d).

3.2. Effect of Gas Composition on the Nanocone Morphology. The results of the experiments on the growth of carbon nanocones in the plasmas with various gas compositions are shown in Figure 4. From this figure one can see that the use of the plasma containing 10–30% of hydrogen results in the synthesis of shorter nanocones which form an array with a higher surface density (Figure 4a–c). Interestingly, the nanocones are more isolated and do not form “nests” visible in Figure 2, though still reshape while growing closely to each other. When no hydrogen is used but the nitrogen content is increased to 60%, the nanocones show a pyramidal shape (Figure 4d,e).

As can be seen in Figures 2 and 4, the nanocones are not uniform in size and the size distribution (of both base diameters and heights) is quite wide. It should be noted that a much more uniform distribution may be achieved by forming a uniform array of the copper catalyst particles before carbon deposition, using, e.g., patterning techniques.¹⁸ In our case, a wide distribution of the nanocone sizes may be considered as an advantage for the applications demonstrated below (in section 3.5), since the wide size and gap distribution ensures effective trapping of light of various wavelengths and adsorption of molecules of various sizes.

To check the composition, Raman characterization was performed for the four samples, i.e., the reference sample synthesized in the $\text{CH}_4 + \text{N}_2$ gas mixture with the CH_4/N_2 ratio of 1:1 and the three samples described above. These spectra for the samples grown in the plasma containing 20, 40, 50, and 60% of nitrogen show clear D and G peaks evidencing that in all cases the nanocone base consists of carbon (Figure 5). Furthermore, the intensity ratio of graphitic peak I_G to disordered peak I_D remains almost constant (~ 0.5) even with increasing nitrogen concentration in the plasma, this revealing that the nitrogen concentration leads to the shape change of the nanocones without deteriorating their graphitic crystalline structure.

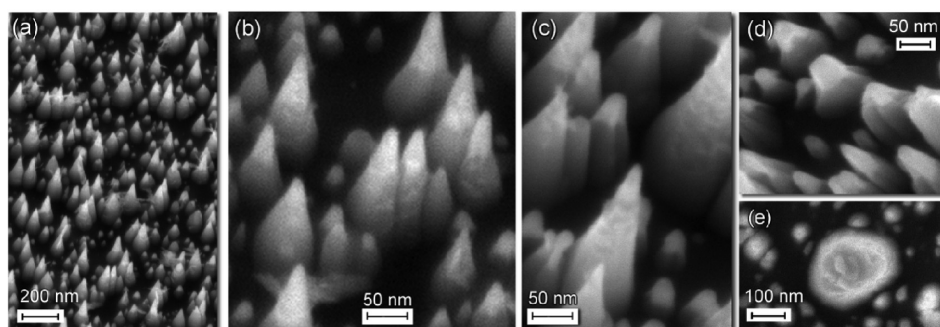


Figure 4. Dependence of the nanocone array morphology on gas composition. SEM image of the samples processed in $\text{CH}_4/\text{H}_2/\text{N}_2$ mixture with the gas ratio 50/30/20 (a, b), 50/10/40 (c), and 40/0/60 (d, e). Nanostructures grown at the power $P = 800$ W and substrate bias -50 V. The arrays grown in the hydrogen-containing plasma consist of shorter nanocones but exhibit a higher surface density (number of nanocones per surface unit). The nanocones grown at an increased nitrogen content (d, e) show a pyramidal shape.

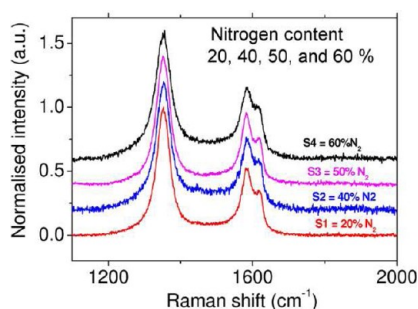


Figure 5. Raman spectra of the four samples grown in the plasma containing 20, 40, 50, and 60% of nitrogen. The intensity ratio of graphitic peak I_G to disordered peak I_D remains almost constant (~ 0.5), thus revealing that the variation of the nitrogen concentration leads to the shape change of the nanocones without deteriorating their graphitic crystalline structure.

3.3. Effect of Ion Energy on the Nanocone Morphology

To investigate the effect of ion energy on the nanocone growth, additional experiments were conducted at floating and -100 V dc surface potential conditions in the reference gas mixture $\text{CH}_4/\text{N}_2 = 50/50$ (Figure 6a,b). The nanocones synthesized on the floating and -100 V biased substrates do not show much difference in the shape. Moreover, the array synthesized on the floating substrate contains long, blunt-ended structures with large, globular copper tops of about 50 nm in diameter (Figure 6a illustrates the typical long blunt nanocone). The array grown at the large (-100 V) surface bias exhibits only sharp-pointed nanocones with the top diameter not exceeding 10–20 nm. Additional characterization for the

samples fabricated at different surface biases have also demonstrated a near-constant intensity I_G/I_D ratio, this evidencing that increasing the substrate bias does not cause defects in their graphitic crystalline structure.

3.4. Remarkable Features of the Nanocone Morphology and Plausible Mechanism of the Structure Formation

The most remarkable feature of the nanocone arrays is a separate growth of the nanostructures, which tend to maintain the gap between them. This can be clearly seen in Figures 2b,c, 4b, and 7. In some cases the gap between the nanocones may be very narrow (not exceeding 10 nm) and very long, exceeding 500 nm in vertical direction (normal to the substrate surface), as shown in Figure 7a. Another observation is that the nanocones in the groups reshape and form a faceted shape to lean closely to each other without a direct contact with each other, whereas the two remote nanocones grow symmetrically into two nanocones with round-shaped bases (Figure 7b,c). On the other hand, when the two nanocones are located at a center-to-center distance comparable with the base radius, the radial growth toward the neighboring nanocone stops when the gap between the two nanostructures decreases to several nm, and the faceted shape (triangular or semi-rounded from one side, as seen in Figure 7b) eventually forms. The vertical growth continues as seen in Figure 7a, so very long nanostructures grow still maintaining the gap between them.

In our previous work we have discussed the possible reasons for such growth behavior and have proposed the growth mechanism based on the assumption of the effective formation of the hydrocarbons in the plasma.¹³ Specifically, we have pointed out that a noncoalescing growth behavior shows that some additional process ensures the stability of smaller

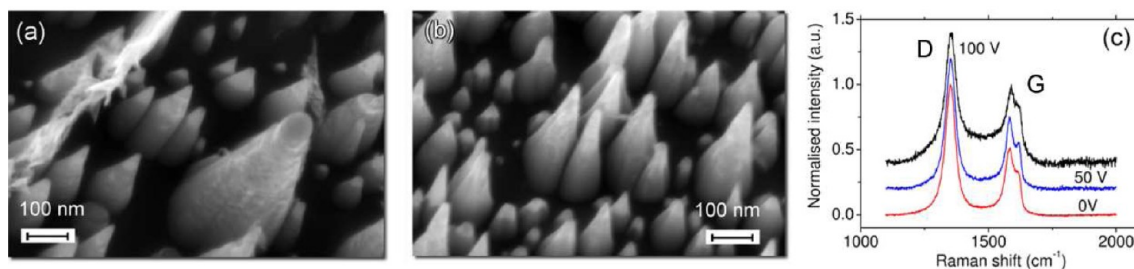


Figure 6. Dependence of the nanocone array morphology on the substrate bias. Reference gas mixture ($\text{CH}_4/\text{N}_2 = 50/50$). Floating substrate (a) and -100 V dc bias (b). Raman spectra of the three samples grown at 0, -50 , and -100 V dc show clear D and G peaks evidencing that in all cases the nanocone base consists of carbon. The intensity ratio of graphitic peak I_G to disordered peak I_D remains almost constant (~ 0.5), thus revealing that the variation of the substrate bias leads to the shape change of the nanocones without deteriorating their graphitic crystalline structure.

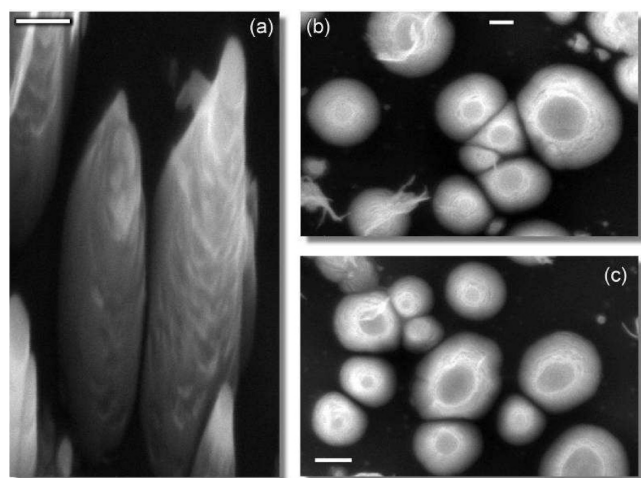


Figure 7. SEM image (side view) of the closely-located separated nanocones, showing very narrow (about 10 nm) gaps between the nanocone walls (a) and two nanocone configurations (SEM images, top view) showing very narrow gaps between the nanostructures (b, c). These configurations were selected for modeling. Scale bars are 100 nm.

nanostructures by changing the energy balance on the nanostructure surface in narrow gaps, and thus the energy minimization-driven coalescence does not take place. Furthermore, we have pointed out that in the high-density $\text{CH}_4 + \text{N}_2$ plasma with the electron temperature reaching several electronvolts the conditions for the synthesis of various hydrocarbons including higher hydrocarbons such as $\text{C}_n\text{H}_{2n+2}$ are favorable.^{19–21} Further, we have estimated the sheath width between the plasma bulk and the substrate surface to be of several tens of micrometers, thus significantly exceeding the nanocone length. On the basis of these estimates, we have concluded that the electric field in the sheath cannot provide effective ion bombardment of the nanocone surfaces in gaps, and hence, higher hydrocarbons can be effectively formed in the gaps thus changing the surface energy of nanostructures and eventually “banning” the coalescence.

Another interesting observation is the reshaping of the closely located nanostructures which acquire a pyramidal-like shape (Figure 4d,e) at the increased hydrogen content in the reactive environment. We explain this reshaping of the nanocones by effective termination of the dangling bonds on the nanostructure surface, which results in a change of the surface energy. We have already demonstrated in our previous works that the hydrogen content in the reactive mixture is an effective tool for controlling the surface energy of nanostructures that grow under nonequilibrium conditions.²¹ We assume that for the carbon nanocones considered, a quite similar mechanism is responsible for the reshaping in the plasma.

Another pathway that potentially could drive the coalescence is the redistribution of the deposited material on the substrate surface due to surface diffusion. If this process is intense enough, i.e., surface diffusion can sustain a substantial amount of the adsorbed material on the substrate surface in the gaps between the nanostructures, the coalescence could take place even on passivated surfaces, via possible reaction of the hydrocarbons with the adsorbed material (note the process was conducted at elevated temperatures 500–600 °C). Otherwise, depleted zones (free of the adsorbed material) should be found between the nanostructures, and thus, the coalescence should

not be possible due to the absence of building material required for the growth.

It should be noted that the unusual morphology of the arrays, namely, the presence of very narrow gaps between the nanostructures, makes them very promising for application in optics (since the gaps may work as effective light traps) and also as a platform for the sensing devices where the narrow gap may be filled and short-circuited with a large single molecule such as, e.g., protein. With these potential applications in a view, we have conducted two special experiments demonstrating the possibility of the nanocone application in optical and biosensing devices.

3.5. Potential Applications of the Carbon-Capped Nanocone Arrays. Arrays of long nanocones can be effectively used as a reflectance-alternating coating. Figure 8

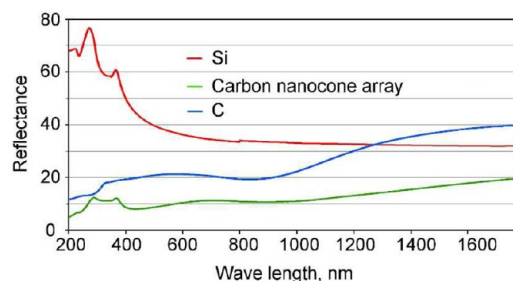


Figure 8. Spectral reflectance of the carbon nanocone array compared with that of a bare Si wafer and amorphous carbon, showing a significantly lower reflectance in the broad spectral range.

shows the results of the spectral reflectance measurements of the carbon nanocone array, compared with that of a bare Si wafer. For comparison, the graph also shows the spectral reflectance of amorphous C. The response of the carbon nanocone array follows the response of C, indicating that C is predominant on the surface. There is also evidence of the underlying Si substrate, particularly at UV wavelengths. Importantly, the carbon nanocone array shows approximately a half of the reflectance of C in the broad spectral range. This is at least partially due to much lower scattering from the surface (the spectral measurements were of specular reflectance at close to normal incidence, not including diffuse reflectance) but may also include light trapping due to the conical morphology of the nanostructured surface. The efficient refractive index measurement based on the Brewster angle gave a value of $n \approx 1.26$ at 633 nm, which is approximately half that of amorphous carbon (~ 2.43).

Other promising application of the arrays of metal-capped nanocones is biosensing.²² To check the applicability of these structures for detecting biomolecules (e.g., proteins), we have performed a set of dedicated measurements (see the schematic in Figure 9a). A model sensing platform was based on as-prepared dense film of carbon nanocones, with the two silver electrodes (separated by a 8-mm gap) deposited on the substrate. The electrical resistance measurements were performed using a physical property measurement system (PPMS). The phosphate buffered saline (PBS) buffer with pH value of 7.2 was first applied to the platform, and then 1% w/v bovine serum albumin (BSA) was added using a PBS buffer solution. The graph in Figure 9b shows the change in the resistance of the carbon nanocone film in the presence of PBS and 1% of BSA proteins with time. After loading PBS, the resistance of the film decreases. Upon further addition of 1%

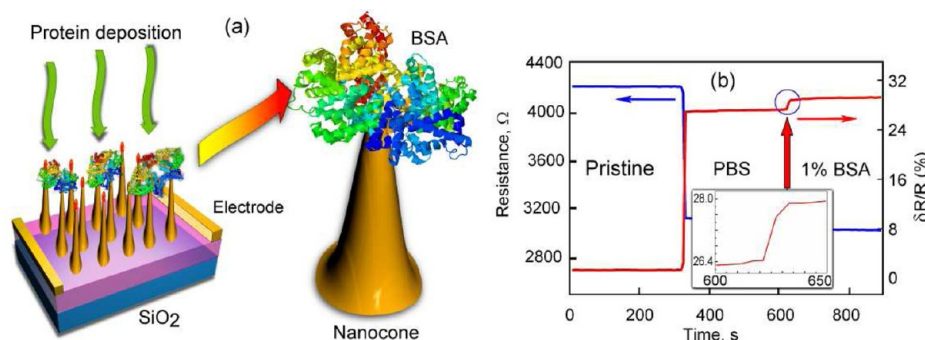


Figure 9. Schematic of the protein sensing measurements (a). Protein solution is applied to the nanocone array, and the change in the resistance is measured using a pair of silver electrodes. The graph (b) quantifies the measured change in the resistance. The inset shows the resistance drop after BSA application.

w/v BSA solution, an additional resistance drop was also detected (at 600 s). From this graph one can conclude that the PBS filled the gaps between the nanocones and thus reduced the resistance by 20%. When the protein solution was added to the film, the proteins are likely to attach to the copper tip and cause a further small change in the film resistance. Thus, the copper-capped nanocone film is highly promising as a possible biosensing platform.

4. NUMERICAL MODELING

As we have mentioned in section 3, the formation of narrow gaps between the nanostructures is a feature important for the practical applications of the nanostructure array. To support our assumptions about the mechanism responsible for the formation of gaps between nanocones, we have conducted hybrid numerical simulations which made it possible to prove the mechanism proposed.

We have selected two typical configurations (groups) of the closely located nanocones that show narrow gaps between them (these groups are shown in Figure 7b,c). For these configurations we have designed numerical models and used them to calculate the density field of the adsorbed atoms (adatoms) on the substrate surface between the nanocones. The surface processes were simulated using the model based on the surface diffusion equation for the adatom density field $\eta(x, y, t)$ on the substrate surface

$$\frac{\partial \eta}{\partial t} = D_s \left(\frac{\partial^2 \eta}{\partial x^2} + \frac{\partial^2 \eta}{\partial y^2} \right) + \psi_{in,i} + \psi_{in,0} - \psi_{vp} + \psi_O \quad (1)$$

where D_s is the surface diffusion coefficient; $\psi_{in,0}$ and $\psi_{in,i}$ are the external fluxes of neutrals and ions to the substrate surface, respectively; ψ_{vp} is the evaporation flux from the substrate surface; x, y are the Cartesian coordinates; and ψ_O is the term that account for other processes.

The evaporation flux from the substrate surface can be calculated as

$$\psi_{vp} = \frac{S}{\lambda_a^2} \nu_0 \exp(\epsilon_s/kT_s) \quad (2)$$

where ϵ_s is the energy of atom evaporation from the substrate surface to the 3D vapor, k is the Boltzmann's constant, λ_a is the lattice constant, ν_0 is the frequency of lattice atom oscillations, S is the surface area, and T_s is the surface temperature. The distribution of the external flux of building materials to the substrate surface ψ_{in} was assumed to be uniform, according to our above-mentioned estimate which has shown that the sheath

width is large enough compared with the nanocone height. The surface diffusion coefficient was taken in the form

$$D_s = \frac{\lambda_a \nu_0}{4} \exp(\epsilon_d/kT_s) \quad (3)$$

where ϵ_d is the surface diffusion activation energy. Similarly, we have taken into account the following surface processes that can be described in terms of diffusion and used for calculation of ψ_O : flux of adatoms to the nanocones, evaporation of adatoms from the nanocones to the plasma, and evaporation of adatoms from the nanocones to the substrate surface. The external flux of neutrals to the substrate surface, $\psi_{in,0}$, was calculated as $\psi_{in,0} = V_0 P / (kT_g)$, where V_0 is the neutral particle velocity at the gas temperature T_g and pressure P .

The distribution of the ion flux $\psi_{in,i}$ in the pattern of long nanostructures was calculated taking into account the electric field distribution in the presheath/sheath and the ion motion from the bulk plasma–sheath border through the sheath to nanostructure or substrate particle surface. In presheath, the electric potential distribution is

$$\phi_{PS(x)} = \phi_0 \left(\frac{x + \bar{\lambda}}{\bar{\lambda}} \right)^2 \quad (4)$$

where ϕ_0 is the electric potential at the sheath/presheath boundary, $\bar{\lambda}$ is the presheath thickness, and x is the distance to the boundary from the current point. The total potential drop in the presheath is small, so we will not consider in details the ion motion in the presheath but instead will just use the presheath potential drop for obtaining the ion energy at the boundary which often is assumed to correspond to the Bohm velocity $V_B = (eT_e/m)^{1/2}$,²³ where T_e is the electron temperature and m is the atom mass. The electric field distribution $\phi_S(x)$ in the sheath can be obtained in analytic form as $\phi_S(x) = \phi_B(x/\lambda)^{4/3}$, where ϕ_B is the surface bias potential. Finally, in the vicinity of the substrate surface covered with the nanotube array, the electric field should be obtained by integrating the distribution of uncompensated electric charge in the sheath $\rho(x,y,z)$ (Poisson equation) $\epsilon_0 \Delta \phi(x,y,z) = -\rho e(x,y,z)$. After calculation a complete distribution of the electric potential in the pattern, the ion velocity can be calculated:

$$v_i(t) = v_i(0) + \int_0^t (eE/m_i) d\tau \quad (5)$$

using the distribution of electric field in the sheath: $\mathbf{E}(x,y,z) = \nabla \phi(x,y,z)$.

Finally, the explicit trajectory can be obtained by integrating eq 5. This system was solved using the Monte Carlo technique. The trajectory of each ion was traced separately from the presheath–sheath border than through the sheath until collision with the nanotube or substrate surface, and the information about hit point coordinates was accumulated in a 2D data matrix for collisions with the substrate surface and in a number in vector files for collisions with the nanotubes. Some more detail on the model and calculation technique can be found elsewhere.^{5,19} Numerical simulations were conducted for the parameters measured in the experiment (see Table 1 for the

Table 1. Main Simulation Parameters

parameter	notation	value
nanostructure radii	r_m	50–250 nm
nanostructure height	H	1000 nm
no. of nanostructures in the pattern	N_n	1000
electron temperature in the low-temperature plasma	T_e	2–5 eV
plasma density	n_p	up to 10^{16} m^{-3}
sheath width	λ_h	$8 \times 10^{-4} \text{ cm}$
neutral gas temperature	T_g	300 K
neutral gas pressure	P	5 Pa
process duration	t	15 min
substrate bias	U_s	50–100 V
total substrate area	S_s	$1000 \text{ nm} \times 1000 \text{ nm}$
surface temperature	T_s	600 °C
ion energy at the sheath edge	ϵ_i	1.0 eV
no. of ions in Monte Carlo simulation	N_i	2×10^5
frequency of lattice atom oscillations	ν_0	$3.3 \times 10^{13} \text{ s}^{-1}$
discharge power	W	800 W

complete list of parameters). The results of the calculations of the adatom density field for the two nanocone configurations are shown in Figure 10a,c. A half-tone map of the density field shows that the density is nearly uniform on the substrate surface remote from the nanostructures (a balance of the particle influx from the plasma and evaporation to the plasma only sustains a relatively high density). The density is lower in the areas located closely to the nanocones, and the lowest densities are found in the narrow gaps between the nanocones. To better illustrate this, we have made a 3D reconstruction of the nanocone patterns with the calculated density fields, Figure 10b,d. From these images one can clearly see that the zero-density adatom-free zones are formed between the nanocones. The adatoms cannot penetrate into these zones by surface diffusion, since the long diffusion path requires long surface residence time, and adatoms evaporate from the surface during this travel. On the other hand, as it was already mentioned, direct deposition from the plasma to the density-depleted zones cannot sustain a noticeable density of adatoms in the gaps, since the plasma-surface sheath is much larger than the nanocone length and thus the ions cannot be drawn directly into the gaps by the electric field.

Figure 11 illustrates the calculated electric field in nanostructure groups shown in Figure 10. The calculations were made by numerically solving the Poisson equation in the sheath at the vicinity of the substrate surface. From this image one can see that the field is very strong around the free-standing nanocones (the strongest field is found near the nanostructure walls), but it is very weak between the two adjacent nanostructures. This eventually results in a very low

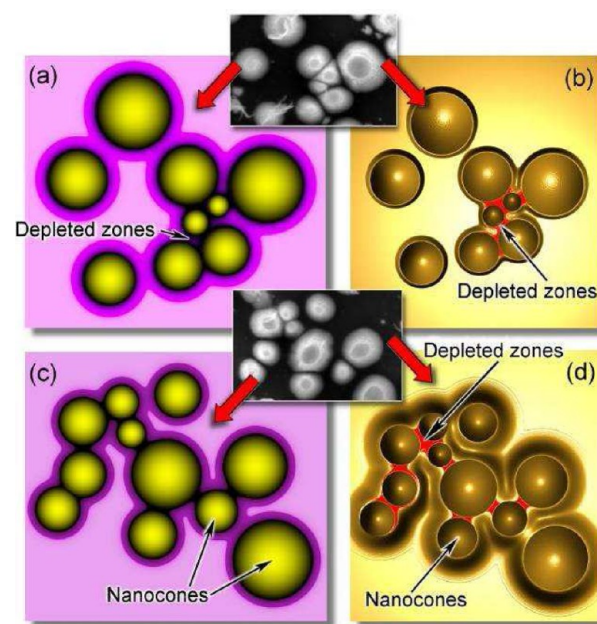


Figure 10. Two nanocone configurations (SEM images on insets) selected for modeling: model configurations with the calculated fields of the adatom density around nanocones (a, c) and 3D representations of the model configurations with the adatom density-depleted zones (b, d). Scale bars are 100 nm.

density of adsorbed atoms in the gaps, as shown in Figure 10b,d.

Therefore, we have demonstrated by the numerical simulations that redistribution of the deposited material on the substrate surface by surface diffusion also cannot cause the coalescence of the growing nanocones, since the zero-density zones are formed on the substrate surface between the nanocones. As a result, (i) no effective material supply into the gaps between the growing nanocones is possible; (ii) conditions for the effective synthesis of hydrocarbons are present in the dense plasma, and thus the nanocones in the gaps (where the ion bombardment is weak) can be passivated. This in turn changes the surface energy of the growing nanostructures and eventually hampers the coalescence.

On the basis of the results of the calculations and the above conclusions, we propose the two-stage growth mechanism that is consistent with the experimental results and simulations. First, when all nanocones are free-standing and do not interact with each other, an effective hydrogen termination of the side surfaces serves as a factor promoting the nanostructure growth to form tall and sharp nanocones.²⁴ At the second stage, small gaps are formed between some nanocones and, simultaneously, their temperature increases due to the strong ion flux-associated heating. As a result, plasma-generated hydrocarbon molecules form a hydrocarbonized layer on the nanocone walls in the gap between the nanocones. As a result, any penetration and incorporation of the carbon material into the nanocone from that side becomes impossible and the radial growth toward the nearly contacting nanocone stops. Meanwhile, ion bombardment (which can reactivate the surface by removing the passivating species) becomes ineffective due to a very narrow gap between the nanocones, and the penetration of any species from the substrate surface by surface diffusion also becomes ineffective. In the experiments when a higher concentration of nitrogen was used, and hence a strong nitrogen flux to the

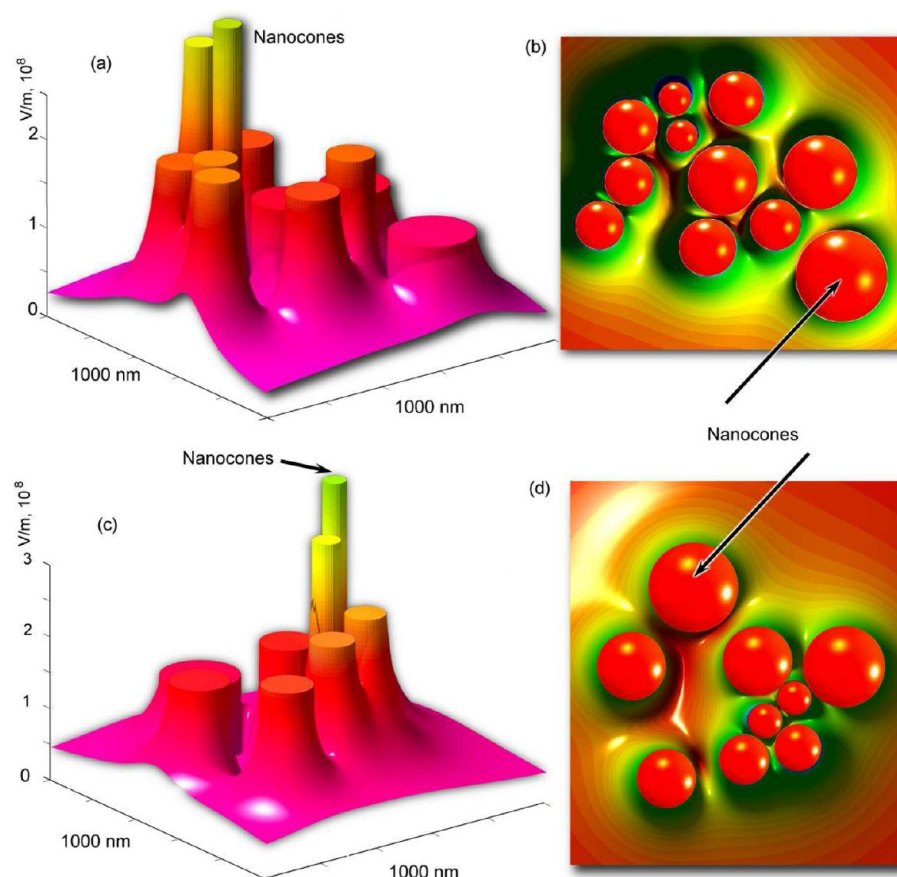


Figure 11. 3D representations (a, c) and top view of the calculated electric field (b, d) in the two patterns shown in Figure 10. The field is strong around the free-standing nanocones but is very weak between the two adjacent nanostructures. This results in the very low density of adsorbed atoms in the gaps.

nanocones was generated, the nanocones were reshaped as seen in Figure 4d. These experiments have also shown that the nanocones can coalesce when the nitrogen density is higher.

5. CONCLUSIONS

In summary, we have demonstrated a very effective plasma-enabled process for the fabrication of clearly separated, vertically aligned carbon nanocones capped with copper nanoparticles. The gaps between the nanocones can be effectively controlled by the gas composition and the surface bias. The use of the hydrogen-enriched environment results in the formation of the denser arrays of shorter nanocones. It was also demonstrated that the arrays grown at a -100 V surface bias exhibit only sharp-pointed nanocones. Optical measurements have demonstrated lower reflectance of the nanocone array in the visible light range (at the wavelength comparable with the length of the nanocones). Thus, components potentially suitable for the use in the nanoelectronic, nanomechanic, microfluidic, optoelectronic, sensing, energy conversion, and other applications can be fabricated.

AUTHOR INFORMATION

Corresponding Author

*E-mail: Igor.Levchenko@csiro.au. Phone: +61-2-9413-7173.

Author Contributions

[†]These authors contributed equally.

Notes

The authors declare no competing financial interest.

ACKNOWLEDGMENTS

This project was partially supported by the Australian Research Council and CSIRO's OCE Science Leadership Program. This work was supported in part by the NSF/DOE Partnership in Plasma Science and Technology (NSF Grant CBET-0853777, DOE Grant DE-SC0001169). The authors thank M. Gross for his valuable help in optical measurements.

REFERENCES

- (1) Robinson, J. T.; Jorgolli, M.; Shalek, A. K.; Yoon, M.-H.; Gertner, R. S.; Park, H. *Nat. Nanotechnol.* **2012**, *7*, 180.
- (2) Suh, M.; Meyyappan, M.; Ju., S. *Nanotechnology* **2012**, *23*, 305203.
- (3) Ostrikov, K. *Rev. Mod. Phys.* **2005**, *77*, 489.
- (4) Bendall, J. S.; Graz, I.; Lacour, S. P. *ACS Appl. Mater. Interfaces* **2011**, *3* (8), 3162.
- (5) Knaapila, M.; Rømoen, O. T.; Svåsand, E.; Pinheiro, J. P.; Martinsen, Ø. G.; Buchanan, M.; Skjeltorp, A. T.; Helgesen, G. *ACS Appl. Mater. Interfaces* **2011**, *3* (2), 378.
- (6) Levchenko, I.; Ostrikov, K. *Nanotechnology* **2008**, *19*, 335703.
- (7) Shieh, J.; Lin, C. H.; Yang, M. C. *J. Phys. D: Appl. Phys.* **2007**, *40*, 2242.
- (8) Calahorra, Y.; Greenberg, Y.; Cohen, S.; Ritter, D. *Nanotechnology* **2012**, *23*, 245603.
- (9) Shashurin, A.; Keidar, M. *Carbon* **2008**, *46*, 1826.
- (10) Mariotti, D. *Appl. Phys. Lett.* **2008**, *92*, 151505.
- (11) Kersten, H.; Thieme, G.; Fröhlich, M.; Bojic, D.; Tung, D. H.; Quaas, M.; Wulff, H.; Hippler, R. *Pure Appl. Chem.* **2005**, *77*, 415.

- (12) Melechko, A. V.; McKnight, T. E.; Guillorn, M. A.; Merkulov, V. I.; Ilic, B.; Doktycz, M. J.; Lowndes, D. H.; Simpson, M. L. *Appl. Phys. Lett.* **2003**, *82*, 976.
- (13) Kumar, S.; Levchenko, I.; Keidar, M.; Ostrikov, K. *Appl. Phys. Lett.* **2010**, *97*, 151503.
- (14) Ostrikov, K.; Seo, D. H.; Mehdipour, H.; Cheng, Q.; Kumar, S. *Nanoscale* **2012**, *4*, 1497.
- (15) Han, Z. J.; Yick, S.; Levchenko, I.; Tam, E.; Yajadda, M. M. A.; Kumar, S.; Martin, P. J.; Furman, S.; Ostrikov, K. *Nanoscale* **2011**, *3*, 3214.
- (16) Wolter, M.; Levchenko, I.; Kersten, H.; Ostrikov, K. *Appl. Phys. Lett.* **2010**, *96*, 133105.
- (17) Tsakadze, Z. L.; Levchenko, I.; Ostrikov, K.; Xu, S. *Carbon* **2007**, *45*, 2022.
- (18) Choi, W. K.; Liew, T. H.; Dawood, M. K.; Smith, H. I.; Thompson, C. V.; Hong, M. H. *Nano Lett.* **2008**, *8*, 3799.
- (19) Mao, M.; Bogaerts, A. *J. Phys. D: Appl. Phys.* **2010**, *43*, 315203.
- (20) Denysenko, I.; Ostrikov, K. *Appl. Phys. Lett.* **2007**, *90*, 251501.
- (21) Levchenko, I.; Huang, S. Y.; Ostrikov, K.; Xu, S. *Nanotechnology* **2010**, *21*, 025605.
- (22) Sotiropoulou, S.; Chaniotakis, N. A. *Anal. Bioanal. Chem.* **2003**, *375*, 103.
- (23) Keidar, M.; Beilis, I. I. *EEE Trans. Plasma Sci.* **2005**, *33*, 1481.
- (24) Levchenko, I.; Ostrikov, K.; Long, J. D.; Xu, S. *Appl. Phys. Lett.* **2007**, *91*, 113115.